Quantum oscillations in acoustic phonons of nodal-line semimetals

Hao-Jie Lin,[1,2,3,4] Tianyu Liu,[1,4] and Hai-Zhou Lu[1,2,3,4,*]

[1]*Shenzhen Institute for Quantum Science and Engineering and Department of Physics, Southern University of Science and Technology (SUSTech), Shenzhen 518055, China*

[2]*Quantum Science Center of Guangdong-Hong Kong-Macao Greater Bay Area (Guangdong), Shenzhen 518045, China*

[3]*Shenzhen Key Laboratory of Quantum Science and Engineering, Shenzhen 518055, China*

[4]*International Quantum Academy, Shenzhen 518048, China*

(Received 26 January 2024; revised 29 March 2024; accepted 1 May 2024; published 13 May 2024)

We theoretically investigate the magnetoacoustic oscillation and the attenuation oscillation of long-wavelength acoustic phonons in nodal-line semimetals. Because of the electron-phonon interaction, we observe pronounced oscillatory behaviors in the dispersion modification and attenuation of acoustic phonons at low temperatures. These oscillations, exhibiting unique patterns associated with Fermi surface and magnetic field directions, serve as direct manifestation of both the Fermi-surface geometry and relativistic features of electrons. Our findings propose that these observed oscillations offer discernible signatures for characterizing the electronic structures of the nodal-line semimetals.

DOI: 10.1103/PhysRevB.109.195421

I. INTRODUCTION

Nodal-line semimetals represent a subset of topological semimetals characterized by the emergence of a symmetry-protected degenerate nodal line or ring formed through the intersection of the valence and conduction bands [1–8]. Their topology is labeled by a π Berry phase accumulated along a contour interlocking the nodal line or ring [9]. In addition to the distinctive characteristics exhibited by the bulk bands, nodal-line semimetals feature unique topological drumhead surface states capable of hosting special transport properties [10–13]. Quite a few materials have been identified as nodal-line semimetals, including $TlTaSe_2$ [12], $PbTaSe_2$ [14], ZrSiS [15–17], $PtSn_4$ [18], and $ZrTe_5$ [19] with very low carrier density.

Quantum oscillation [20] serves as a potent tool for the investigation of nodal-line semimetals. As a canonical magnetic response, the electronic states in nodal-line semimetals are fundamentally reorganized into Landau levels, which pass through the Fermi surface under a scanned magnetic field, thus giving rise to oscillations in density of states and so many other associated properties (conductivity, magnetization, magnetic torque, Seebeck coefficient, thermopower, etc.). Specifically, the Shubnikov-de Haas oscillation has been employed to elucidate the Fermi-surface topology, relativistic nature, and scattering mechanism of nodal-line semimetals [19,21–32]. The de Haas-van Alphen oscillation and magnetic torque oscillation techniques are able to unravel the Fermiology of nodal-line semimetals [33–37] with reduced sensitivity to disorder, allowing direct comparison with the Lifshitz-Kosevich formula [20,38,39]. The thermoelectric quantum oscillation provides an alternative approach resolving the Fermi-surface morphology and can also probe the effective mass and phonon effects [40–42].

Despite the systematic study on the quantum oscillations of electrons in nodal-line semimetals, the magnetic transport of phonons in nodal-line semimetals remains elusive. Recent studies have remarkably illustrated the magnetic transport of phonons in Weyl [43,44] and Dirac [45–48] semimetals in the form of magnetoacoustic and phonon attenuation oscillations, where the electron-phonon interaction plays the key role passing the quantum oscillations from electrons to phonons. With the magnetic transport of phonons being clarified in nodal-point semimetals [43–48] and the electron-phonon interaction in nodal-line semimetals [49–55] becoming increasingly notable, it would be natural to investigate the phonon oscillations in nodal-line semimetals. Moreover, this approach not only enables the extraction of electronic features but also contributes to a deeper understanding of the electron-phonon interaction [56,57]. More intriguingly, even in the presence of smearing mechanisms, the phonon attenuation oscillation in the nodal-line semimetals would be more retainable than the Shubnikov-de Haas and de Haas-van Alphen oscillations and can provide more precise field locations of the peaks of the oscillatory properties. Considering these advantages, there is a significant demand for theoretical exploration of phonon magnetic oscillations in nodal-line semimetals.

In this paper, we explore the magnetoacoustic and attenuation oscillations of the long-wavelength acoustic phonons in nodal-line semimetals. This exploration details the effects of the electron-phonon interaction on the phonon dispersion modification $\Delta\Omega_q$ and the phonon attenuation Γ_q at low temperatures. Our observations reveal that, depending on the position of the Fermi level, both $\Delta\Omega_q$ and Γ_q exhibit distinct oscillatory behaviors with respect to the applied magnetic field. Under a scanned out-of-plane magnetic field, their oscillations show beating (monochromatic) patterns when

*Corresponding author: luhz@sustech.edu.cn

the Fermi level lies in the regime of a torus (drum-like) Fermi surface. This finding suggests that the oscillations of acoustic phonons can provide insights into the Fermi-surface geometry and are legitimate alternatives for the electron quantum oscillations. Under a scanned in-plane magnetic field, we analytically derive the Landau levels and show that the oscillations of topologically trivial phonons can acquire a topologically nontrivial phase shift from electrons. This discovery greatly advances our understanding of electron-phonon interaction in nodal-line semimetals.

The paper is organized as follows. In Sec. II, we introduce the minimal model of nodal-line semimetals and the formal theory of phonon dispersion modification and attenuation. In Sec. III, we present the magnetoacoustic oscillation of phonon dispersion modification. In Sec. IV, the giant quantum oscillation of phonon attenuation is explored. Section V concludes the paper and briefly discusses the experimental accessibility of phonon quantum oscillations and their advantages over the electron quantum oscillations.

II. MODEL AND FORMAL THEORY

We first present the minimal Hamiltonian describing the nodal-line semimetals [12,14,58–60],

$$H = \left[M_1\left(k_x^2 + k_y^2\right) - M_0\right]\sigma_z + \lambda k_z \sigma_x, \tag{1}$$

where $\boldsymbol{k} = (k_x, k_y, k_z)$ is the wave vector; M_1, M_0, and λ are the model parameters. To host a nodal-line semimetal phase, parameters should satisfy $M_0 M_1 > 0$. Without loss of generality, we set $M_0 > 0$ and $M_1 > 0$. The topology is originated from the parity-symmetry-breaking second term associated with k_z. The energy dispersion of Eq. (1) reads $E_\pm = \pm\{\lambda^2 k_z^2 + [M_0 - M_1(k_x^2 + k_y^2)]^2\}^{1/2}$, from which a nodal ring with radius $\sqrt{M_0/M_1}$ is found at the zero energy and $k_z = 0$. There are two distinct types of Fermi surfaces associated with different values of the Fermi energy μ. For $|\mu| < M_0$, the above dispersion yields a torus Fermi surface [Figs. 1(a) and 1(c)], whereas for $|\mu| > M_0$, a drum-like Fermi surface emerges [Fig. 1(b)]. On the interface $|\mu| = M_0$, the hole of the torus Fermi surface closes and leaves a node at $\boldsymbol{k} = 0$ [Fig. 1(d)].

We now construct the formal theory of phonon quantum oscillations. We here focus on the magnetoacoustic oscillation of phonon dispersion modification $\Delta\Omega_q$ and the giant oscillation of phonon attenuation Γ_q in the presence of scanned out-of-plane and in-plane magnetic fields (respectively labeled as $\boldsymbol{B}_\perp$ and $\boldsymbol{B}_\parallel$). The oscillatory properties are respectively derived as

$$\Delta\Omega_q = \Re[\Pi^R(\boldsymbol{q}, \Omega_q)], \quad \Gamma_q = -\Im[\Pi^R(\boldsymbol{q}, \Omega_q)], \tag{2}$$

where $\Pi^R(\boldsymbol{q}, \Omega_q)$ is the retarded self-energy of long-wavelength acoustic phonons.

To derive the above retarded self-energy, we begin with the investigation of electron-phonon interaction. We here only consider the orbital effect (i.e., the Landau quantization) of electrons subjected to the applied magnetic field, while disregarding the Zeeman effect. For the long-wavelength acoustic phonons, the dispersion $\Omega_q = v_p q$ is taken to be linear in momentum $\boldsymbol{q} = (q_x, q_y, q_z)$ with v_p being associated with the phonon velocity. Within the Fermi liquid regime, the

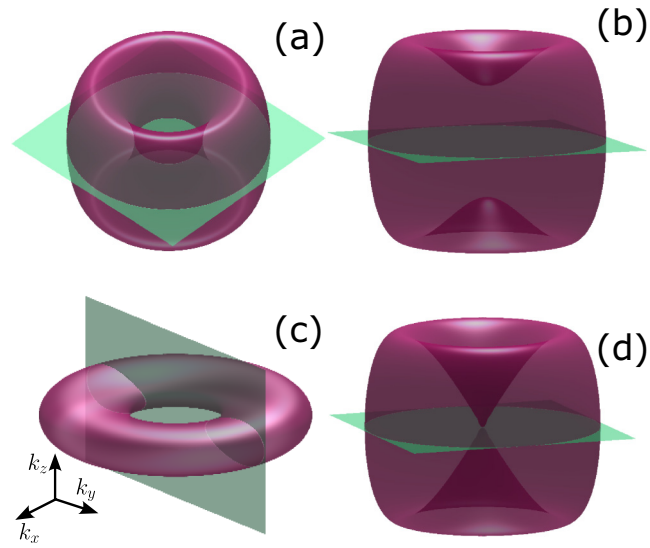

FIG. 1. Fermi surfaces of the nodal-line semimetal [Eq. (1)]. (a) Torus Fermi surface with $|\mu| < M_0$. The intersecting plane shows the maximal and minimal cross sections in the presence of an out-of-plane (i.e., z direction) magnetic field. (b) Drum-like Fermi surface with $|\mu| > M_0$. The intersecting plane displays the maximal cross section in the presence of an out-of-plane magnetic field. (c) Torus Fermi surface with $|\mu| < M_0$. The intersecting plane highlights the minimal cross section with two circular regions in the presence of an in-plane (i.e., x direction) magnetic field. (d) Fermi surface on the interface between torus and drum-like Fermi surfaces with $|\mu| = M_0$. The intersecting plane marks the vanishing point of the minimal cross section under an out-of-plane magnetic field. For all panels, we set the model parameters $M_0 = 0.1$ eV, $M_1 = 0.38$ eV nm^2, and $\lambda = 1$ eV nm.

electron-phonon interaction is formulated as

$$V_{\rm ep} = \sum_{\alpha,\beta}\sum_{\boldsymbol{q}} \Gamma^{(0)}_{\alpha\beta} a^\dagger_\alpha a_\beta (b^\dagger_{-\boldsymbol{q}} + b_{\boldsymbol{q}}), \tag{3}$$

where α, β represent the quantum numbers such as Landau level index, band index, and electron momentum; $a^\dagger_\alpha$ (a_α) is the creation (annihilation) operator for an electron in the quantum state $|\alpha\rangle$ with energy ε_α; $b^\dagger_{\boldsymbol{q}}$ ($b_{\boldsymbol{q}}$) is the creation (annihilation) operator for a long-wavelength acoustic phonon with momentum $\boldsymbol{q}$ and energy Ω_q. The interaction vertex is

$$\Gamma^{(0)}_{\alpha\beta}(\boldsymbol{q}) = \langle\alpha|U(\boldsymbol{q})e^{-i\boldsymbol{q}\cdot\boldsymbol{r}}|\beta\rangle, \tag{4}$$

where $U(\boldsymbol{q})$ is the electron-phonon perturbation potential. For simplicity, $U(\boldsymbol{q})$ is assumed to be irrelevant to electrons [i.e., $U(\boldsymbol{q})$ exhibits no α dependence]. In fact, it has been acknowledged that $U(\boldsymbol{q})$ in general relies on the phonon momentum, the phonon velocity, and crystal properties as $|U(\boldsymbol{q})|^2 = 4\pi^2\chi$ with $\chi = \hbar^2 D^2 q/(8\pi^2 v_p \rho)$, where D is the deformation potential constant and ρ is the mass density of the crystal [61].

We then derive the phonon self-energy based on the electron-phonon interaction. The Dyson equation for the phonon Green's function is [62]

$$\mathcal{D}^{-1}(\boldsymbol{q}, \Omega) = \mathcal{D}_0^{-1}(\boldsymbol{q}, \Omega) - \Pi(\boldsymbol{q}, \Omega), \tag{5}$$

where $\mathcal{D}_0^{-1}(\boldsymbol{q}, \Omega) = 2\Omega_q/(\Omega^2 - \Omega_q^2)$ is the free phonon Green's function and $\Pi(\boldsymbol{q}, \Omega)$ is the phonon self-energy

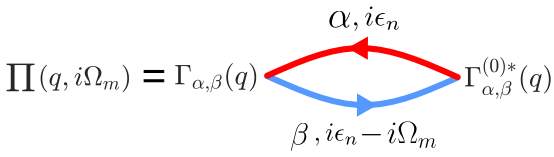

FIG. 2. The bubble diagram of phonon self-energy.

enclosing the interaction rectification to the free phonons. To find the explicit form of the phonon self-energy, we adopt the Matsubara formalism. In the imaginary frequency domain, the phonon self-energy is illustrated in the bubble diagram (see Fig. 2) as

$$\Pi(\boldsymbol{q}, i\Omega_m) = \frac{k_B T}{V} \sum_{i\varepsilon_n} \sum_{\alpha\beta} G(\alpha, i\varepsilon_n)\Gamma_{\alpha\beta}(\boldsymbol{q}) \times G(\beta, i\varepsilon_n - i\Omega_m)\Gamma^{(0)*}_{\alpha\beta}(\boldsymbol{q}), \tag{6}$$

where $V = L_x L_y L_z$ is the volume of the nodal-line semimetal; and $\Omega_m = 2m\pi k_B T$ and $\varepsilon_n = (2n+1)\pi k_B T$ with $n, m \in \mathbb{Z}$ are the Matsubara bosonic and fermionic frequencies, respectively.

Lastly, we derive the retarded phonon self-energy from the bubble diagram (see Fig. 2). To the lowest order, the electron-phonon interaction vertex and the electron Green's function can be substituted by $\Gamma^{(0)}_{\alpha\beta}(\boldsymbol{q})$ and $G^{(0)}(\alpha, i\varepsilon_n) = (i\varepsilon_n - \varepsilon_\alpha + \mu)^{-1}$, respectively. After summing over the imaginary frequency $i\varepsilon_n$ [62], the retarded phonon self-energy can be expressed by performing the substitution $i\Omega_m \to \Omega_q + i\delta$. Explicitly, it reads

$$\Pi^R(\boldsymbol{q}, \Omega_q) = \frac{1}{V} \sum_{\alpha\beta} \Gamma^{(0)}_{\alpha\beta}\Gamma^{(0)*}_{\alpha\beta} \frac{n_F(\xi_\alpha) - n_F(\xi_\beta)}{\varepsilon_\alpha - \varepsilon_\beta - \Omega_q - i\delta}, \tag{7}$$

where δ is a positive infinitesimal parameter, $\xi_{\alpha,\beta} = \varepsilon_{\alpha,\beta} - \mu$, and $n_F(\xi_{\alpha,\beta}) = 1/\exp[\xi_{\alpha,\beta}/(k_B T) + 1]$ is the Fermi-Dirac distribution. The interaction vertex part is further written as $\Gamma^{(0)}_{\alpha\beta}\Gamma^{(0)*}_{\alpha\beta} = |U(\boldsymbol{q})|^2 |\mathcal{F}_{\alpha\beta}(\boldsymbol{q})|^2$. It contains two individual components, in which $|U(\boldsymbol{q})|^2$ only depends on phonons whereas $|\mathcal{F}_{\alpha\beta}(\boldsymbol{q})|^2 = |\langle\alpha|e^{-i\boldsymbol{q}\cdot\boldsymbol{r}}|\beta\rangle|^2$ also relies on the eigenstates of electrons (i.e., $|\alpha\rangle$ and $|\beta\rangle$).

In the rest of this section, we will derive the electronic eigenstates of the nodal-line semimetals [Eq. (1)] subjected to two different magnetic fields: (i) the out-of-plane magnetic field $\boldsymbol{B}_\perp$; and (ii) the in-plane magnetic field $\boldsymbol{B}_\parallel$. With the eigenstates resolved, we calculate for each field orientation $|\mathcal{F}_{\alpha\beta}(\boldsymbol{q})|^2$ and consequently $\Pi^R(\boldsymbol{q}, \Omega_q)$, with which the phonon dispersion modification and attenuation can be obtained by making use of Eq. (2).

A. Out-of-plane magnetic field

With a uniform magnetic field perpendicular to the nodal ring plane, i.e., along the z direction as $\boldsymbol{B}_\perp = (0, 0, B)$, the corresponding vector potential can be chosen as $\boldsymbol{A}_\perp = (-By, 0, 0)$. In the search for eigenvalues, we adopt the trial wave function $(c_1|\nu\rangle, c_2|\nu\rangle)^T$. By solving the associated

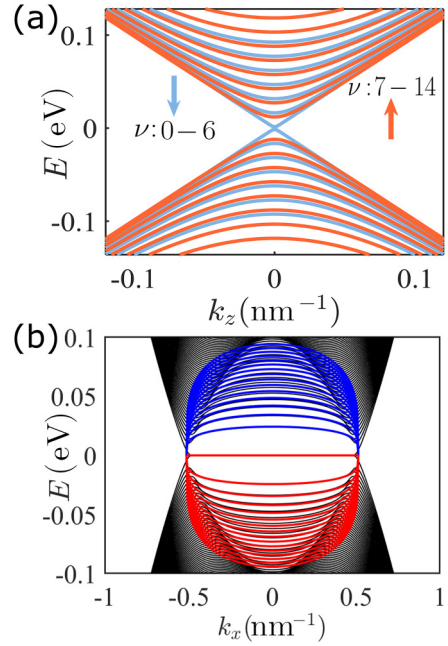

FIG. 3. Landau levels of the nodal-line semimetal [Eq. (1)]. (a) Landau levels in the presence of an out-of-plane (i.e., z direction) magnetic field $B_\perp = 13.1$ T. In the $E > 0$ regime showed, the energy bands comprises Landau levels indexed by $\nu = 0, \cdots, 6$ from top to bottom (blue) and Landau levels indexed by $\nu = 7, \cdots, 14$ from bottom to top (red). As the magnetic field increases, the former will first move downward and then rise up, while the latter consistently ascend. (b) Landau levels in the presence of an in-plane (i.e., x direction) magnetic field $B_\parallel = 1$ T. The black bands are obtained from the diagonalization of Eq. (1), wherein the in-plane magnetic field is incorporated through the Peierls substitution with the vector potential $\boldsymbol{A}_\parallel$. The blue and red bands correspond to the approximate low-energy Landau levels [Eq. (26)]. The model parameters are $M_0 = 0.1$ eV, $M_1 = 0.38$ eV nm^2, and $\lambda = 1$ eV nm for panel (a) [$\lambda = 0.5$ eV nm for p(b)].

secular equation, the Landau level dispersion Fig. 3(a) reads

$$\varepsilon^{\nu s}_{k_z} = s\sqrt{\left[\hbar\omega\left(\nu + \frac{1}{2}\right) - M_0\right]^2 + \lambda^2 k_z^2}, \tag{8}$$

where $s = \pm$ labels the conduction and valence bands, ν is the Landau level index, and $\omega = 2M_1 eB/\hbar^2$ is the cyclotron frequency. The corresponding eigenvectors can be written as

$$|s, \nu, k_x, k_z\rangle = \begin{pmatrix} C^{\nu s}_{k_z} \\ D^{\nu s}_{k_z} \end{pmatrix} |\nu, k_x, k_z\rangle, \tag{9}$$

where $C^{\nu+}_{k_z} = -D^{\nu-}_{kz} = \cos\theta^{k_z}_\nu/2$ and $C^{\nu-}_{k_z} = D^{\nu+}_{k_z} = \sin\theta^{k_z}_\nu/2$ with $\cos\theta^{k_z}_\nu = [\hbar\omega(\nu + 1/2) - M_0]/\varepsilon^{\nu+}_{k_z}$. The Landau level wave function $\psi_{\nu,k_x,k_z}(\boldsymbol{r}) = \langle\boldsymbol{r}|\nu, k_x, k_z\rangle$ reads

$$\psi_{\nu,k_x,k_z}(\boldsymbol{r}) = \frac{\tilde{C}_{\nu,k_x,k_z}}{\sqrt{L_x L_z \ell_B}} e^{-\frac{(y-y_0)^2}{2\ell_B^2}} \mathcal{H}_\nu\left(\frac{y - y_0}{\ell_B}\right), \tag{10}$$

where $\tilde{C}_{\nu,k_x,k_z} = C_\nu e^{ik_x x} e^{ik_z z}$ is the normalized prefactor with $C_\nu = 1/\sqrt{\nu! 2^\nu \sqrt{\pi}}$; $L_{x(z)}$ measures the sample dimension along the x (z) direction; $y_0 = k_x \ell_B^2$ is the Landau level guiding center with the magnetic length $\ell_B = \sqrt{\hbar/eB}$; and $\mathcal{H}_\nu(\cdot)$ is the

νth Hermite polynomial. The solutions to the lowest Landau levels can be found via setting $\nu = 0$. Note that the lowest Landau levels are located around $\pm M_0$ rather than the charge neutrality point [Fig. 3(a)].

With the aid of the explicit eigenvectors [Eq. (9)], $\mathcal{F}_{\alpha\beta}(\boldsymbol{q})$ is obtained as

$$\mathcal{F}_{\alpha\beta}(\boldsymbol{q}) = M(\boldsymbol{q})[C^{\nu s}_{k_z} C^{\nu' s'}_{k'_z} + D^{\nu s}_{k_z} D^{\nu' s'}_{k'_z}]\mathcal{J}^{\nu'}_{\nu}(u) \times \delta_{k_x+q_x,k'_x}\delta_{k_z+q_z,k'_z}, \tag{11}$$

where the coefficients $C^{\nu s}_{k_z}$ and $D^{\nu s}_{k_z}$ are inherited from Eq. (9), and the parameters $\mathcal{J}^{\nu'}_{\nu}$ and $M(\boldsymbol{q})$ are respectively defined as

$$\mathcal{J}^{\nu'}_{\nu}(u) = \sqrt{u}^{|\nu'-\nu|}\sqrt{\frac{\min(\nu,\nu')!}{\max(\nu,\nu')!}}L^{|\nu'-\nu|}_{\min(\nu,\nu')}(u),$$
$$M(\boldsymbol{q}) = e^{i\varphi_q(\nu'-\nu)}e^{-iq_y(y'_0+y_0)/2}e^{-u/2}. \tag{12}$$

For transparency, we define in Eq. (12) $u = \frac{1}{2}\ell_B^2 q_\parallel^2$ with $q_\parallel^2 = q_x^2 + q_y^2$, $\varphi_q = \arctan(q_y/q_x)$, and $L^m_N(x)$ is the associated Laguerre polynomial.

It is now necessary to contemplate the constraints imposed by the long-wavelength condition on the aforementioned equations. For acoustic phonons with wavelength much larger than the magnetic length (i.e., $q\ell_B \ll 1$), the dominant contribution to $\mathcal{F}_{\alpha\beta}(\boldsymbol{q})$ is from the intraband transitions (i.e., $\nu' = \nu$) near the Fermi surface. This is understandable as the phonon momentum $\boldsymbol{q}$ is small, preventing the transition between different bands, which are far apart [63]. Consequently, to the leading order, it is legitimate to write $\mathcal{J}^{\nu'}_{\nu}(u) \approx \delta_{\nu,\nu'}$, $M(\boldsymbol{q}) \approx 1$, $C^{\nu s}_{k_z} \approx C^{\nu s}_{k_z+q_z}$, and $D^{\nu s}_{k_z} \approx D^{\nu s}_{k_z+q_z}$. Making use of Eqs. (11) and (12), we obtain

$$|\mathcal{F}_{\alpha\beta}(\boldsymbol{q})|^2 = \delta_{k'_x,k_x}\delta_{k'_z,k_z+q_z}\delta_{\nu,\nu'}\delta_{s,s'}, \tag{13}$$

which, upon plugging into Eq. (7), results in the retarded phonon self-energy

$$\Pi^R(\boldsymbol{q},\Omega_q) = \frac{\chi}{\ell_B^2}\sum_{\nu,s}\int dk_z \frac{n_F(\xi^{\nu s}_{k_z}) - n_F(\xi^{\nu s}_{k_z+q_z})}{\varepsilon^{\nu s}_{k_z} - \varepsilon^{\nu s}_{k_z+q_z} - \Omega_q - i\delta}. \tag{14}$$

Note that the Ω_q in the denominator, although tiny, must not be neglected, because the amplitude of $\varepsilon^{ns}_{k_z} - \varepsilon^{ns}_{k_z+q_z}$ is comparable to Ω_q. By definition [Eq. (2)], the finite-temperature modification of phonon dispersion and the finite-temperature phonon attenuation respectively read

$$\Delta\Omega_q = \frac{\chi}{\ell_B^2}\sum_{\nu,s}\int dk_z \frac{n_F(\xi^{\nu s}_{k_z}) - n_F(\xi^{\nu s}_{k_z+q_z})}{\varepsilon^{\nu s}_{k_z} - \varepsilon^{\nu s}_{k_z+q_z} - \Omega_q}, \tag{15}$$
$$\Gamma_q = \frac{\pi\chi}{\ell_B^2}\sum_{\nu,s}\int dk_z\big[n_F(\xi^{\nu s}_{k_z+q_z}) - n_F(\xi^{\nu s}_{k_z})\big] \times \delta\big(\varepsilon^{\nu s}_{k_z} - \varepsilon^{\nu s}_{k_z+q_z} - \Omega_q\big), \tag{16}$$

which are nonzero exclusively when q_z possesses a finite value, in accordance with the conservation of momentum and energy (i.e., $k'_z = k_z + q_z$ and $\varepsilon^{\nu'}_{k'_z} = \varepsilon^{\nu}_{k_z} + \Omega_q$, respectively).

We now further simplify Eqs. (15) and (16). Considering that the long-wavelength approximation forbids the interband transition and requires a small q_z, the numerator and the denominator of the integrand of Eq. (15) can be respectively parameterized in terms of θ, the angle between the phonon propagation and the applied magnetic field [i.e., $\theta = \arccos(q_z/q)$ for $\boldsymbol{B}_\perp$], as

$$n_F(\xi^{\nu s}_{k_z}) - n_F(\xi^{\nu s}_{k_z+q_z}) \approx q\hbar\cos\theta\, v^{\nu s}_{k_z}\delta(\varepsilon^{\nu s}_{k_z} - \mu),$$
$$\varepsilon^{\nu s}_{k_z} - \varepsilon^{\nu s}_{k_z+q_z} - \Omega_q \approx -\big(v^{\nu s}_{k_z}\cos\theta + v_p/\hbar\big)q\hbar, \tag{17}$$

where we assume zero temperature such that n_F becomes a Heaviside function and the electron velocity is defined as $v^{\nu s}_{k_z} = d\varepsilon^{\nu s}_{k_z}/(\hbar dk_z)$. Hence, the phonon dispersion modification [Eq. (15)] and the phonon attenuation [Eq. (16)] are respectively simplified to

$$\Delta\Omega_q = -\frac{\chi}{\ell_B^2}\sum_{\nu,s}\int dk_z \frac{v^{\nu s}_{k_z}\cos\theta}{v^{\nu s}_{k_z}\cos\theta + \frac{v_p}{\hbar}}\delta(\xi^{\nu s}_{k_z}), \tag{18}$$
$$\Gamma_q = \frac{\pi\chi v_p}{\ell_B^2\hbar}\sum_{\nu,s}\int dk_z\delta\Big(v^{\nu s}_{k_z}\cos\theta + \frac{v_p}{\hbar}\Big)\delta(\xi^{\nu s}_{k_z}), \tag{19}$$

which indicate that only the electrons near the Fermi surface (i.e., $\xi^{\nu s}_{k_z} = \varepsilon^{\nu s}_{k_z} - \mu \simeq 0$) contribute significantly to the phonon dispersion modification $\Delta\Omega_q$ and attenuation Γ_q. The dispersion modification and attenuation are both proportional to phonon momentum q, a dependence acquired from $\chi = \hbar^2 D^2 q/(8\pi^2 v_p\rho)$. In particular, Γ_q shows singularities periodically when the condition $v^{\nu s}_{k_z}\cos\theta + v_p/\hbar = 0$ is satisfied. It is worth noting that both $\Delta\Omega_q$ and Γ_q are suppressed for $\boldsymbol{q} \perp \boldsymbol{B}$ (i.e., $\theta = \frac{\pi}{2}$), because the both integrands in Eqs. (18) and (19) vanish for $\cos\theta = 0$. Such suppression can also be verified from the phonon absorption. Specifically, because of the intraband transition (i.e., $\nu' = \nu$) and the momentum conservation (i.e., $k'_z = k_z + q_z$), we can expand the Landau level dispersion $\varepsilon^{\nu'}_{k'_z}$ to the first order as $\varepsilon^{\nu'}_{k'_z} \approx \varepsilon^{\nu}_{k_z} + \lambda^2 k_z q_z/\varepsilon^{\nu}_{k_z}$. The energy conservation (i.e., $\varepsilon^{\nu'}_{k'_z} = \varepsilon^{\nu}_{k_z} + \Omega_q$) further gives rise to

$$k_z = \frac{v_p\varepsilon^{\nu}_{k_z}}{\lambda^2}\frac{1}{\cos\theta}. \tag{20}$$

In such a situation only electrons with infinite k'_zs can absorb the phonons if $\boldsymbol{q} \perp \boldsymbol{B}$ (i.e., $\theta = \frac{\pi}{2}$, or, equivalently, $\cos\theta = 0$). Therefore, in the following, we will primarily focus on the parallel propagation case $\boldsymbol{q} \parallel \boldsymbol{B}$ (i.e., $\theta = 0$), unless otherwise specified. It is important to emphasize that our key findings remain applicable even when θ deviates slightly from zero.

B. In-plane magnetic field

We now present the formal theory of phonon transport in the presence of an in-plane magnetic field. Without loss of generality, we adapt Eq. (1) with the rotation $\sigma_z \to \sigma_x$, $\sigma_x \to \sigma_y$. Applying an x direction magnetic field $\boldsymbol{B}_\parallel = (B, 0, 0)$ arising from the vector potential $\boldsymbol{A}_\parallel = (0, -Bz, 0)$, the minimally coupled model Hamiltonian reads

$$H = \Big[M_1 k_x^2 + M_1\Big(k_y - \frac{e}{\hbar}Bz\Big)^2 - M_0\Big]\sigma_x - i\lambda\partial_z\sigma_y. \tag{21}$$

In the low-energy regime, the Landau level guiding centers can be found by requiring the absence of the high-energy terms [64–66] as

$$z_0 = \ell_B^2\big(k_y \pm \sqrt{M_0/M_1 - k_x^2}\big), \tag{22}$$

which indicates two Landau level guiding centers relying on k_x and k_y. The two guiding centers can be understood by examining the extremal cross section of the torus Fermi surface perpendicular to the applied in-plane magnetic field. Such a cross section comprises two separated circular regions [Fig. 1(c)] with distinct momenta, their guiding centers therefore differ. Meanwhile, we note that k_x is confined inside the nodal ring as k_x^2 is less than M_0/M_1. When k_x^2 reaches the threshold M_0/M_1, the two guiding centers merge together.

We here focus on the low-energy theory by linearizing Eq. (21) in the vicinity of the guiding centers as

$$H_\tau = \tau g(z - z_0)\sigma_x - i\lambda\partial_z\sigma_y, \tag{23}$$

where $\tau = \pm$ labels the two distinct guiding centers and $g = 2\sqrt{M_0M_1 - M_1^2k_x^2/\ell_B^2}$ is defined for transparency. To diagonalize H_τ, we consider the following quantum oscillator ladder operators:

$$\begin{aligned} a &= \frac{1}{\sqrt{2}}\left[\sqrt{\frac{g}{\lambda}}(z - z_0) + \sqrt{\frac{\lambda}{g}}\frac{\partial}{\partial z}\right], \\ a^\dagger &= \frac{1}{\sqrt{2}}\left[\sqrt{\frac{g}{\lambda}}(z - z_0) - \sqrt{\frac{\lambda}{g}}\frac{\partial}{\partial z}\right], \end{aligned} \tag{24}$$

with which the Hamiltonian [Eq. (23)] of the two distinct guiding centers become

$$H_+ = \sqrt{2\lambda g}\begin{bmatrix} 0 & a^\dagger \\ a & 0 \end{bmatrix}, \quad H_- = -\sqrt{2\lambda g}\begin{bmatrix} 0 & a \\ a^\dagger & 0 \end{bmatrix}. \tag{25}$$

In terms of $|n\rangle$, the eigenstates of the number operator $a^\dagger a$ (i.e., $a^\dagger a|n\rangle = n|n\rangle$), the eigenenergies and eigenstates of H_τ are

$$\begin{aligned} H_+ &: \ E_{k_x}^{ns} = s\sqrt{2n\lambda g}, \quad \psi_s^{(+)} = \frac{1}{\sqrt{2}}\begin{bmatrix} |n\rangle \\ s|n-1\rangle \end{bmatrix}, \\ H_- &: \ E_{k_x}^{ns} = s\sqrt{2n\lambda g}, \quad \psi_s^{(-)} = \frac{1}{\sqrt{2}}\begin{bmatrix} |n-1\rangle \\ s|n\rangle \end{bmatrix}, \end{aligned} \tag{26}$$

where $s = \pm$ specifies the conduction and valence bands and the superscript $(\pm)$ labels the guiding centers. The analytic Landau level dispersion is substantiated by the good match to the numerics [Fig. 3(b)]. The harmonic wave function $\psi(n, k_x, k_y, z) = \langle \boldsymbol{r}|n\rangle$ explicitly reads

$$\psi(n, k_x, k_y, z) = \frac{C_n\ell_{k_x}^{-1/4}}{\sqrt{L_xL_y}}e^{-\frac{(z-z_0)^2}{2\ell_{k_x}^2}}H_n\left(\frac{z - z_0}{\ell_{k_x}}\right), \tag{27}$$

where $C_n = e^{ik_xx}e^{ik_yy}/\sqrt{n!2^n\sqrt{\pi}}$ and $\ell_{k_x} = \sqrt{\lambda/g}$ is analogous to the magnetic length ℓ_B.

Following the same procedure deriving $|\mathcal{F}_{\alpha\beta}(\boldsymbol{q})|^2$ in the presence of an out-of-plane magnetic field, we obtain

$$|\mathcal{F}_{\alpha\beta}(\boldsymbol{q})|^2 = \delta_{k_y',k_y}\delta_{k_x',k_x+q_x}\delta_{n,n'}\delta_{s,s'}, \tag{28}$$

which can be alternatively obtained by rotating the directions of the momenta in Eq. (13) according to $z \to x$, $x \to y$, because we have adopted the rotation $\sigma_z \to \sigma_x$, $\sigma_x \to \sigma_y$ to Eq. (1). Note that the Landau level indices in Eq. (28) are denoted as n and n', different from those (i.e., ν and ν') in Eq. (13). Plugging Eq. (28) into Eq. (7), we find the retarded phonon self-energy as

$$\Pi^R(\boldsymbol{q}, \Omega_q) = \frac{\chi'}{\ell_B^2}\sum_{n,s}\int dk_x \frac{n_F\left(\Xi_{k_x}^{ns}\right) - n_F\left(\Xi_{k_x+q_x}^{ns}\right)}{E_{k_x}^{ns} - E_{k_x+q_x}^{ns} - \Omega_q - i\delta}, \tag{29}$$

where we define $\Xi_{k_x}^{ns} = E_{k_x}^{ns} - \mu$ and $v_p' = v_p/2$ in the parameter $\chi' = \hbar^2D^2q/(8\pi^2v_p'\rho)$. Alternatively, Eq. (29) can be mapped from the retarded phonon self-energy under an out-of-plane magnetic field [Eq. (14)] by momentum rotation $k_z, q_z \to k_x, q_x$ and Landau level dispersion substitution $\varepsilon_{k_z}^{\nu s} \to E_{k_x}^{ns}$. By definition [Eq. (2)], the finite-temperature phonon dispersion modification and attenuation respectively reads

$$\Delta\Omega_q = \frac{\chi'}{\ell_B^2}\sum_{n,s}\int dk_x \frac{n_F\left(\Xi_{k_x}^{ns}\right) - n_F\left(\Xi_{k_x+q_x}^{ns}\right)}{E_{k_x}^{ns} - E_{k_x+q_x}^{ns} - \Omega_q}, \tag{30}$$

$$\begin{aligned} \Gamma_q = \frac{\pi\chi'}{\ell_B^2}\sum_{n,s}\int dk_x &\left[n_F\left(\Xi_{k_x}^{ns}\right) - n_F\left(\Xi_{k_x+q_x}^{ns}\right)\right] \\ &\times \delta\left(E_{k_x}^{ns} - E_{k_x+q_x}^{ns} - \Omega_q\right), \end{aligned} \tag{31}$$

which are parallel to Eqs. (15) and (16). At zero temperature, the dispersion modification [Eq. (30)] and attenuation [Eq. (31)] can be further simplified as

$$\Delta\Omega_q = -\frac{\chi'}{\ell_B^2}\sum_{n,s}\int dk_x \frac{v_{k_x}^{ns}}{v_{k_x}^{ns} + \frac{v_p}{\hbar}}\delta\left(\Xi_{k_x}^{ns}\right), \tag{32}$$

$$\Gamma_q = \frac{\pi\chi' v_p'}{\ell_B^2\hbar}\sum_{n,s}\int dk_x \delta\left(v_{k_x}^{ns} + \frac{v_p}{\hbar}\right)\delta\left(\Xi_{k_x}^{ns}\right), \tag{33}$$

where $v_{k_x}^{ns} = \partial E_{k_x}^{ns}/(\hbar\partial k_x)$. Equations (32) and (33) constitutes an analogy to Eqs. (18) and (19) with momentum rotation and Landau level dispersion substitution. Note that we here have already set $\theta = 0$, because the phonon absorption can only be pronounced when the phonon propagation and the magnetic field are parallel, as analyzed in Sec. II A.

III. MAGNETOACOUSTIC OSCILLATION OF PHONON DISPERSION MODIFICATION

This section delves into the oscillatory behaviors of the phonon dispersion modification for both the out-of-plane and in-plane magnetic fields. We here focus on the semiclassical regime, where the quantum oscillation is induced by many Landau levels passing through the Fermi surface. We will show that the oscillation of phonon dispersion modification, also known as the magnetoacoustic oscillation, is as powerful as the Shubnikov-de Haas and de Haas-van Alphen oscillations in resolving the Fermi-surface morphology and the topological characteristics of electrons.

A. Out-of-plane magnetic field

In the presence of an out-of-plane magnetic field, the zero-temperature phonon dispersion modification [Eq. (18)] exhibits singularities when the velocity of phonons is canceled by the electron velocity in the direction of the magnetic field. This cancellation usually happens at the momenta k_z's where the energy bands become rather flat, because the electron velocity is usually much lager than the phonon velocity

(typically by three orders). Away from the momenta where singularities take place, the phonon dispersion modification is further simplified as

$$\Delta\Omega_q = -\frac{\chi}{\ell_B^2}\int dk_z \mathcal{A}(k_z), \tag{34}$$

where, in terms of $\varepsilon_{\nu k_z} = \varepsilon_{k_z}^{\nu+}$, the integrand reads

$$\mathcal{A}(k_z) = 2|\mu|\sum_{\nu=0}^{\infty}\delta\left(\varepsilon_{\nu k_z}^2 - \mu^2\right). \tag{35}$$

The form of $\mathcal{A}(k_z)$ is closely related to the electron density of states at the Fermi level, which oscillates with a scanned out-of-plane magnetic field. Consequently, the phonon dispersion modification [Eq. (34)] relying on $\mathcal{A}(k_z)$ indeed exhibits quantum oscillation, known as the magnetoacoustic oscillation.

Before the analysis of the magnetoacoustic oscillation, we first simplify the phonon dispersion modification [Eq. (34)] by summing over the Landau level index ν in Eq. (35). This is accomplished by using the Poisson's summation rule [43,67] $\sum_{\nu=0}^{\infty}F(\nu) = \frac{1}{2}F(0) + \int_0^{\infty}d\nu\, F(\nu) + 2\sum_{j=1}^{\infty}\int_0^{\infty}d\nu\, F(\nu)\cos(2\pi j\nu)$, where F is an arbitrary function of the integer ν. After performing the summation, the phonon dispersion modification [Eq. (34)] takes the form as

$$\Delta\Omega_q = -\Delta\Omega_q^a - \Delta\Omega_q^b - \Delta\Omega_q^c, \tag{36}$$

where

$$\begin{aligned}
\Delta\Omega_q^a &= \frac{\chi|\mu|}{M_1}\sum_{\ell}\int dk_z \frac{\Theta(n_{\ell,k_z})}{\zeta_{k_z}}\sum_{j=1}^{\infty}\cos(2\pi j n_{\ell,k_z}),\\
\Delta\Omega_q^b &= \frac{\chi}{2\ell_B^2}\int dk_z[\delta(\varepsilon_{0k_z}-\mu)+\delta(\varepsilon_{0k_z}+\mu)],\\
\Delta\Omega_q^c &= \frac{\chi|\mu|}{2M_1}\sum_{\ell}\int dk_z\frac{\Theta(n_{\ell,k_z})}{\zeta_{k_z}}.
\end{aligned} \tag{37}$$

In Eq. (37), Θ is the Heaviside function, $\ell = \pm$, and we define for transparency

$$\begin{aligned}
\zeta_{k_z} &= \sqrt{\mu^2 - \lambda^2 k_z^2},\\
n_{\ell,k_z} &= \frac{\ell_B^2}{2}\frac{M_0 + \ell\zeta_{k_z} - \hbar\omega/2}{M_1}.
\end{aligned} \tag{38}$$

In $\Delta\Omega_q^a$, the sinusoidal part oscillates quickly with respect to k_z because of the large factor ℓ_B^2 in n_{ℓ,k_z}, whereas the prefactor $\Theta(n_{\ell,k_z})/\zeta_{k_z}$ slowly varies with k_z. In the framework of the saddle-point approximation [67], the integration over k_z in $\Delta\Omega_q^a$ is mainly contributed around the extremal points $k_z = k_\ell = 0$, determined by $\partial n_{\ell,k_z}/\partial k_z|_{k_\ell} = 0$. Therefore, $\Delta\Omega_q^a$ is further recast as

$$\Delta\Omega_q^a = \frac{\chi|\mu|}{M_1}\sum_{\ell}\sum_{k_\ell}\sum_{j=1}^{\infty}\frac{\Theta(n_{\ell,k_\ell})}{\zeta_{k_\ell}\sqrt{j|n''_{\ell,k_\ell}|}}\cos\left(2\pi j n_{\ell,k_\ell} \pm \frac{\pi}{4}\right), \tag{39}$$

where the $\pm$ sign corresponds to the sign of $n''_{\ell,k_\ell} = \partial^2 n_{\ell,k_z}/\partial k_z^2|_{k_z=k_\ell}$ [67] and n_{ℓ,k_ℓ} is related to the extremal cross sections via the Lifshitz-Onsager relation $n_{\ell,k_z} = S(k_z,\mu)\ell_B^2/(2\pi) - 1/2$.

We then analyze the magnetoacoustic oscillation in a general sense. For a weak magnetic field, both $\Delta\Omega_q^a$ and $\Delta\Omega_q^b$ become vanishingly small because of the large ℓ_B, while magnetic-field-free $\Delta\Omega_q^c$ is responsible for the phonon

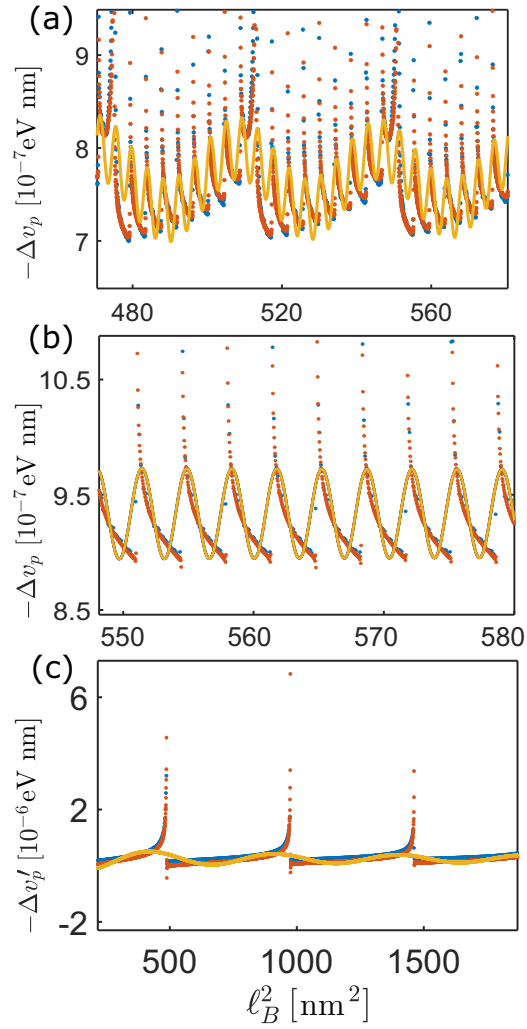

FIG. 4. Magnetoacoustic oscillations. The oscillation is illustrated by the phonon velocity modification (up to a factor of $\hbar$) as a function of ℓ_B^2. The phonon velocity modification is related to the phonon dispersion modification through $\Delta v_p = \Delta\Omega_q/q$. (a) Oscillation for a torus Fermi surface with $\mu = 0.08$ eV in the presence of an out-of-plane magnetic field. The red dots (yellow-dotted curve) are analytical solutions [Eq. (40)] with first 10^4 harmonics (only the first harmonic). (b) Oscillation for a drum-like Fermi surface with $\mu = 0.12$ eV in the presence of an out-of-plane magnetic field. The red dots (yellow-dotted curve) are analytical solutions [Eq. (41)] with first 10^4 harmonics (only the first harmonic). For (a) and (b), the blue dots are the numerical results from Eq. (15) at $T = 100$ mK. (c) Oscillation for a torus Fermi surface with $\mu = 0.04$ eV in the presence of an in-plane magnetic field. The red dots (yellow-dotted curve) correspond to the analytical results derived from Eq. (44) with first 10^4 harmonics (only the first harmonic). The blue dots represent the numerical results from Eq. (30) evaluated at $T = 100$ mK. The parameter values of ZrSiS [49,50,63] are adopted as $D = 5$ eV, $\rho = 4.86\times10^3$ kg/m^3, $q = 10^{-3}$ nm^{-1}, and $v_p = 3.9\times10^{-3}$ eV nm for (a) and (b) [$v_p' = v_p/2 = 1.95\times10^{-3}$ eV nm for (c)].

absorption but shows no quantum oscillations. When the magnetic field is gradually increased, $\Delta\Omega_q^a$ exhibits a multi-frequency quantum oscillation of phonon dispersion modification arising from its sinusoidal part, while $\Delta\Omega_q^b$ and $\Delta\Omega_q^c$ constitute the background of the oscillation with the former contributed by the lowest Landau levels and the latter resembling $\Delta\Omega_q^a$ with $j = 0$. In experiments, the Landau levels responsible for such a magnetoacoustic oscillation are inevitably broadened (e.g., by disorder, scattering, interaction, and finite temperature). Such broadening suppresses the higher harmonics of the magnetoacoustic oscillation and thus makes the effect of the first harmonic [yellow-dotted curves in Figs. 4(a) and 4(b)] stand out [20].

We now substantiate our analytical theory of magnetoacoustic oscillation for the torus [Fig. 1(a)] and drum-like [Fig. 1(b)] Fermi surfaces with numerical simulations. In the numerical simulations, we set $D = 5\,\mathrm{eV}$ and $\rho = 4.86 \times 10^3\,\mathrm{kg/m^3}$ [49], which are typical values for the nodal-line semimetal ZrSiS; and $v_p = 3.9 \times 10^{-3}\,\mathrm{eV\,nm}$ [50] and $q = 10^{-3}\,\mathrm{nm^{-1}}$ [63], which are typical values for the phonon propagation. For the torus Fermi surface, i.e., $|\mu| < M_0$, the phonon dispersion modification [Eq. (36)] can be evaluated as

$$\Delta\Omega_q = -\frac{\pi\chi|\mu|}{M_1\lambda} - \frac{\chi\mathcal{A}_1}{\ell_B}\sum_{j=1}^{\infty}\frac{1}{\sqrt{j}} \times\left[\cos\left(2\pi j\ell_B^2\mathcal{F}_1 - j\pi - \frac{\pi}{4}\right) + \cos\left(2\pi j\ell_B^2\mathcal{F}_2 - j\pi + \frac{\pi}{4}\right)\right], \tag{40}$$

where $\mathcal{F}_1 = (M_0 + |\mu|)/(2M_1)$, $\mathcal{F}_2 = (M_0 - |\mu|)/(2M_1)$, and $\mathcal{A}_1 = \sqrt{2|\mu|/M_1}/\lambda$ are defined for transparency. In Eq. (40), the first term is the background contributed by $\Delta\Omega_q^c$ which only depends on the material parameter λ and the Fermi level $|\mu|$, while the oscillatory sector takes the form of Eq. (39) with the phase shift $-j\pi$ originating from Maslov contribution and the sign difference before $\pi/4$ distinguishing the maximal and minimal cross-sections [68] as illustrated in Fig. 1(a). The two corresponding extremal cross-section areas ($2\pi\mathcal{F}_1$ for the maximal and $2\pi\mathcal{F}_2$ for the minimal) produce oscillations with frequencies $\mathcal{F}_1$ and $\mathcal{F}_2$, respectively. They are visualized as beating patterns in the phonon dispersion modification [Fig. 4(a)]. This double-frequency magnetoacoustic oscillation can also be understood by two sets of Landau levels traversing the Fermi surface in opposite directions. As illustrated in Fig. 3(a), Landau levels with indices $\nu \leqslant 6$ ($\nu \geqslant 7$) cross the Fermi surface from above (below) with an increased magnetic field. The torus Fermi surface breaks down when $|\mu| = M_0$. Consequently, the beating pattern collapses and transforms into a single-frequency magnetoacoustic oscillation, because the oscillatory frequency $\mathcal{F}_2$ vanishes. The absence of minimal cross-section [Fig. 1(d)] semiclassically confirms the resulting single-frequency magnetoacoustic oscillation. For the drum-like Fermi surface, i.e., $|\mu| > M_0$, the phonon dispersion modification [Eq. (36)] can be obtained as

$$\Delta\Omega_q = -\frac{\chi|\mu|}{M_1}\left(\frac{\pi}{\lambda} - \frac{1}{\lambda}\arcsin\frac{\mathcal{P}}{|\mu|}\right) - \frac{\chi|\mu|}{2\ell_B^2}\frac{1}{\lambda\mathcal{P}} - \frac{\chi\mathcal{A}_1}{\ell_B}\sum_{j=1}^{\infty}\frac{1}{\sqrt{j}}\cos\left(2j\pi\ell_B^2\mathcal{F}_1 - j\pi - \frac{\pi}{4}\right), \tag{41}$$

where we define $\mathcal{P} = \sqrt{\mu^2 - (M_0 - \hbar\omega/2)^2}$. The first and second background terms are attributed to $\Delta\Omega_q^c$ and $\Delta\Omega_q^b$, respectively. It is unambiguously found from the last term of Eq. (41) that the magnetoacoustic oscillation is monochromatic [Fig. 4(b)] with the oscillation frequency determined by the maximal cross section of the drum-like Fermi surface [Fig. 1(b)]. Our theory of magnetoacoustic oscillations for the torus [Eq. (40)] and drum-like [Eq. (41)] Fermi surfaces well matches the finite-temperature result [Eq. (15)] and confirms that the magnetoacoustic oscillation can serve as a legitimate alternative to the Shubnikov-de Haas and de Haas-van Alphen oscillations in resolving the Fermi-surface geometry and relativistic nature.

B. In-plane magnetic field

In the presence of an in-plane magnetic field, the zero-temperature phonon dispersion modification is given by Eq. (32). As the electron velocity typically dominates the phonon velocity, the phonon dispersion modification can be further simplified to

$$\Delta\Omega_q' = -\frac{\chi'}{\ell_B^2}\int dk_x\mathcal{A}'(k_x), \tag{42}$$

where, in terms of $E_{nk_x} = E_{k_x}^{n+} = \sqrt{2n\lambda g}$, the integrand reads

$$\mathcal{A}'(k_x) = 2|\mu|\sum_{n=0}^{\infty}\delta\left(E_{nk_x}^2 - \mu^2\right) - \delta(E_{0k_x} + \mu). \tag{43}$$

Since $\mathcal{A}'(k_x)$ and its integration $\Delta\Omega_q'$ are closely related to the electron density of states at the Fermi level, which oscillates with a scanned in-plane magnetic field, we thus expect a magnetoacoustic oscillation. When evaluating $\Delta\Omega_q'$ with Eq. (42), we only consider the Landau levels within the nodal ring [i.e., between the two Dirac-cone-like structures as illustrated in Fig. 3(b)], because it is such Landau levels that make major contribution to the electron density of states and thus the magnetoacoustic oscillation of $\Delta\Omega_q'$. Such magnetoacoustic oscillation is associated with the minimal cross section comprising of two separated but identical circular regions [Fig. 1(c)].

To analyze the magnetoacoustic oscillation, we evaluate the phonon dispersion modification by the Poisson's summation rule and the saddle point approximation [67]. The minimal cross section is picked out for the evaluation. Explicitly, the phonon dispersion modification reads

$$\Delta\Omega_q' \approx -\frac{\chi'|\mu|}{\lambda M_1} - \frac{\mathcal{A}_2}{\ell_B}\sum_{j=1}^{\infty}\frac{1}{\sqrt{j}}\cos\left(2\pi j\ell_B^2\mathcal{F}_3 + \frac{\pi}{4}\right), \tag{44}$$

where we have defined $\chi' = \hbar^2 qD^2/(8\pi^2\rho v_p')$, $\mathcal{A}_2 = 2\chi' M_0[\lambda^{1/2}(M_0M_1)^{3/4}]$ and $\mathcal{F}_3 = \mu^2/[4\lambda(M_0M_1)^{1/2}]$ for

transparency. $\Delta\Omega_q'$ exhibits a single-frequency magnetoacoustic oscillation [Fig. 4(c)] associated with the minimal cross section of the torus Fermi surface [Fig. 1(c)]. Comparing to the phonon dispersion modification under an out-of-plane magnetic field [Eqs. (40) and (41)], the phonon dispersion modification under an in-plane magnetic field [Eq. (44)] exhibits two major differences. On the one hand, the oscillation frequency $\mathcal{F}_3$ exhibits quadratic dependence on the Fermi level rather than the linear dependence in $\mathcal{F}_1$ and $\mathcal{F}_2$. On the other hand, the phase factor has no Maslov contribution $-j\pi$, which is now canceled by the Berry phase inherited from the topology of electron wave functions. We also note that the positive sign before $\pi/4$ confirms the minimal cross-section nature [Fig. 1(c)] of electrons [68]. The magnetoacoustic oscillation encoded in Eq. (44) is numerically justified by its good match to Eq. (30) and should be an alternative for the Shubnikov-de Haas and de Haas-van Alphen oscillations in detecting the Fermiology.

Before we leave this section, we emphasize that our proposed magnetoacoustic oscillation [Eq. (44)] only applies to the torus Fermi surface, because it is derived by making use of the analytic Landau level dispersions [Eq. (26)], which are only valid for Fermi surfaces close to the nodal loop (i.e., $|\mu| \to 0$). For the drum-like Fermi surface, we have $|\mu| > M_0$. Thus, our analytic dispersions [Eq. (26)] become nullified. A more subtle treatment is needed to extract the analytic Landau level dispersions in the presence of an in-plane magnetic field. This would be beyond the scope of the present paper and we thus leave it for future research.

IV. GIANT QUANTUM OSCILLATION OF PHONON ATTENUATION

In this section, we study the semiclassical oscillations of phonon attenuation for both out-of-plane and in-plane magnetic fields. At low temperatures, the phonon attenuation displays a distinctive spike-like pattern oscillating with the magnetic field, commonly referred to as the giant quantum oscillation [20,67,69]. This giant quantum oscillation serves as an alternative to the Shubnikov-de Haas and de Haas-van Alphen oscillations for the detection of Fermi surfaces.

A. Out-of-plane magnetic field

We first study the phonon attenuation at zero temperature [Eq. (19)], where the Dirac delta $\delta(\xi_{k_z}^{\nu s})$ reflects the close connection between the electron density of states at the Fermi level and the phonon attenuation. We thus expect the phonon attenuation produces a giant quantum oscillation under a scanned out-of-plane magnetic field.

Before the analysis of such a giant quantum oscillation, we first simplify the phonon attenuation [Eq. (19)] by mapping the summation over Landau level index ν into an integral with the Poisson's rule [67]. The resulting phonon attenuation becomes

$$\Gamma_q = \frac{\pi\chi v_p}{\ell_B^2\hbar}\sum_s\int dk_z\int_0^\infty d\nu\,\delta\left(\varepsilon_{k_z}^{\nu s}-\mu\right) \times\left[1+2\sum_{j=1}^\infty\cos(2\pi j\nu)\right]\delta\left(v_{k_z}^{\nu s}+\frac{v_p}{\hbar}\right), \tag{45}$$

where $\varepsilon_{k_z}^{\nu s}$ is the Landau level dispersion in the presence of the out-of-plane magnetic field [Eq. (8)] and $v_{k_z}^{\nu s}=\partial\varepsilon_{k_z}^{\nu s}/(\hbar\partial k_z)$. Integrating the two Dirac delta functions over k_z and ν, the phonon attenuation turns into a more compact form

$$\Gamma_q = \frac{\pi\chi v_p|\mu|}{2M_1}\sum_{\ell,i}\left\{\frac{\Theta(n_{\ell,k_z})}{\zeta_{k_z}\left|\partial^2\varepsilon_{k_z}^{ns}/\partial k_z^2\right|_{n_{\ell,k_z}}} \times\left[1+2\sum_{j=1}^\infty\cos(2\pi j n_{\ell,k_z})\right]\right\}_{k_{\ell,i}}, \tag{46}$$

where $\ell=\pm$, n_{ℓ,k_z} is defined in Eq. (38), and $k_{\ell,i}$ represents the ith solution to $v_{k_z}^{ns}=0$. According to Eq. (8), it is straightforward to find $k_{\ell,i}=0$ are the same as the extremal points of the phonon dispersion modification, corresponding to the extremal cross sections. However, the phonon attenuation exhibits two notable distinctions compared to the dispersion modification discussed in Eq. (36). On the one hand, the phonon dispersion modification has a phase shift of $\pm\pi/4$ [cf., Eq. (39)] arising from the saddle-point approximation, while such an extra phase is absent in the attenuation process. On the other hand, the phonon dispersion modification has a factor of $1/\sqrt{j}$, suppressing the contribution from higher-order harmonics, whereas each harmonic is equally significant in the attenuation process. This suggests that the giant quantum oscillation of phonon attenuation can exhibit higher-order harmonics, even when the finite temperature, electron scattering, and sample anisotropy are present.

We then study the phonon attenuation at low but nonzero temperatures. In contrast to evaluating the finite-temperature phonon attenuation [Eq. (16)], we analytically incorporate the temperature effect through convolution [20]. As detailed in Appendix A, the phonon attenuation at low temperature reads

$$\tilde{\Gamma}_q = \frac{\pi\chi v_p|\mu|}{2M_1}\sum_{\ell,i}\left\{\frac{\Theta(n_{\ell,k_z})}{\zeta_{k_z}\left|\partial^2\varepsilon_{k_z}^{ns}/\partial k_z^2\right|_{n_{\ell,k_z}}} \times\left[1+2\sum_{j=1}^\infty\frac{\kappa_j^{\ell,i}\cos(2\pi j n_{\ell,k_z})}{\sinh\left(\kappa_j^{\ell,i}\right)}\right]\right\}_{k_{\ell,i}}, \tag{47}$$

where $\kappa_j^{\ell,i}=2\pi^2 jk_BT(\partial n_{\ell,k_{\ell,i}}/\partial\mathcal{E})_{\mathcal{E}=\mu}$ arises from the convolution and incorporates the finite-temperature effects.

We now substantiate our theory of giant quantum oscillation of phonon attenuation for the torus [Fig. 1(a)] and drum-like [Fig. 1(b)] Fermi surfaces with numerical simulations. For the torus Fermi surface, i.e., $|\mu| < M_0$, the phonon attenuation [Eq. (47)] can be evaluated as

$$\tilde{\Gamma}_q = \Gamma_1\left\{\left[1+2\sum_{j=1}^\infty\frac{\kappa_j\cos(2\pi j\ell_B^2\mathcal{F}_1-j\pi)}{\sinh(\kappa_j)}\right] +\left[1+2\sum_{j=1}^\infty\frac{\kappa_j\cos(2\pi j\ell_B^2\mathcal{F}_2-j\pi)}{\sinh(\kappa_j)}\right]\right\}, \tag{48}$$

where we define the parameters $\Gamma_1=\pi\chi v_p|\mu|/(2\lambda^2M_1)$ and $\kappa_j=\mathrm{sgn}(\mu)\pi^2 j\ell_B^2k_BT/M_1$ for transparency. With a scanned out-plane magnetic field, $\tilde{\Gamma}_q$ exhibits a periodic spike pattern. The frequencies $\mathcal{F}_{1,2}$ of the spike pattern as well as

the Maslov phase $-j\pi$ are the same as those in the phonon dispersion modification [Eq. (40)], but the type of extremal cross sections cannot be determined owing to the absence of phase shift $\pm\pi/4$. The spike pattern displays a decaying amplitude, which, at low temperature $T \ll M_1/(\pi^2\ell_B^2)$, can be approximately derived by replacing the summation over j by an integration and reads

$$2\bar{\Gamma}_q = \Gamma_1 \frac{M_1}{\mathrm{sgn}(\mu)\ell_B^2 k_B T}. \tag{49}$$

It is worth noting that the result of oscillation amplitudes originated from the maximal and minimal cross sections are identical, because they are associated with the same k_z value. Therefore, the two oscillatory branches of Eq. (48) marked with frequencies $\mathcal{F}_1$ and $\mathcal{F}_2$ have the same magnitude $\bar{\Gamma}_q$. These two branches result in two sequences of subpeaks observed in Fig. 5(a). At each of the common multiples of $\mathcal{F}_1$ and $\mathcal{F}_2$, each sequence contributes a subpeak, resulting in a resonance peak with height $2\bar{\Gamma}_q$ [Eq. (49)]. The analytic amplitude [Eq. (49)] well captures the spike pattern numerically evaluated from the finite-temperature theory [Eq. (16)], as illustrated in Fig. 5(a). For the drum-like Fermi surface, i.e., $|\mu| > M_0$, the phonon attenuation [Eq. (47)] can be evaluated as

$$\tilde{\Gamma}_q = \Gamma_1 \left\{ 1 + 2\sum_{j=1}^{\infty} \frac{\kappa_j \cos\left[2\pi j\ell_B^2\mathcal{F}_1 - j\pi\right]}{\sinh(\kappa_j)} \right\}, \tag{50}$$

which exhibits monochromatic giant quantum oscillation with the frequency $\mathcal{F}_1$ being the same as that of the phonon dispersion modification $\Delta\Omega_q$ [Eq. (41)]. The amplitude of the giant quantum oscillation is found to be $\bar{\Gamma}_q$, which well matches the spike pattern numerically predicted by the finite-temperature theory [Eq. (16)], as illustrated in Figs. 5(b) and 5(c). We thus expect our theory of giant quantum oscillation for the torus and drum-like Fermi surfaces to legitimately characterize the Fermi-surface geometry, working as an alternative experimental probe for the Shubnikov-de Haas and de Haas-van Alphen oscillations.

B. In-plane magnetic field

In the presence of an in-plane magnetic field, the phonon attenuation at $T = 0$ is given by Eq. (33), where the Dirac delta $\delta(\Xi_{k_x}^{ns})$ is closely related to the electron density of states at the Fermi level. We thus expect a giant quantum oscillation of phonon attenuation with respect to a scanned in-plane magnetic field.

Following the same procedure detailed in Sec. IV A (i.e., applying Poisson's rule and convolution), the low-temperature phonon attenuation for the torus Fermi surface reads

$$\tilde{\Gamma}'_q = \Gamma_2 \left[1 + 2\sum_{j=1}^{\infty} \frac{\kappa_j \cos\left(2j\pi\ell_B^2\mathcal{F}_3\right)}{\sinh(\kappa_j)} \right], \tag{51}$$

where we define parameters $\Gamma_2 = \pi\chi' v'_p\sqrt{M_0 M_1}/(\lambda M_1^2)$ and $\kappa_j = 2\pi^2 jk_B T\mu\ell_B^2/(2\lambda\sqrt{M_0 M_1})$. Comparing to Eq. (48), the oscillatory part of Eq. (51) exhibits no Maslov phase because of the cancellation from the Berry phase. The magnitude of

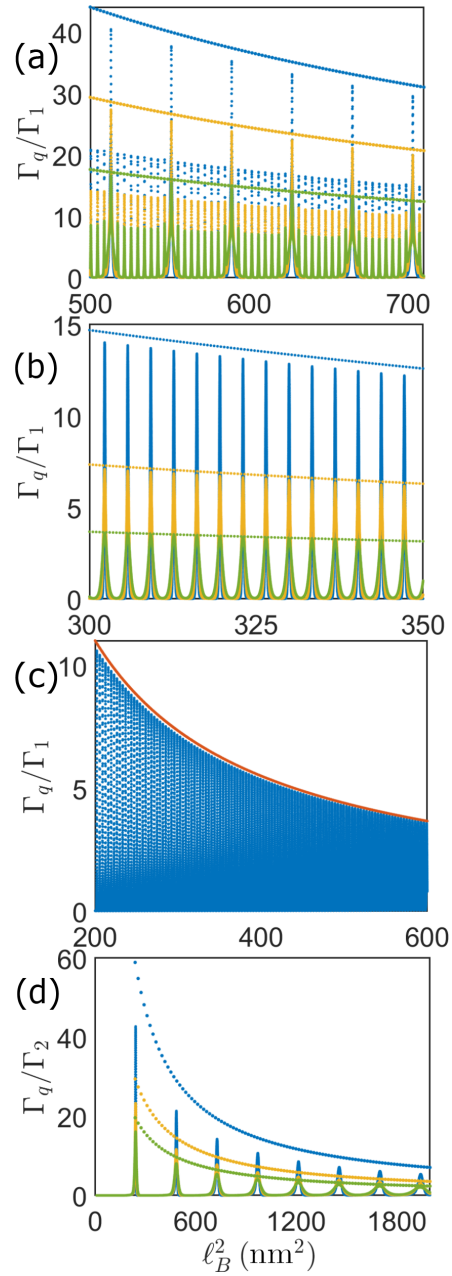

FIG. 5. Giant quantum oscillations of phonon attenuation. (a) Oscillation produced by an out-of-plane magnetic field for a torus Fermi surface with $\mu = 0.08$ eV. The attenuation spike patterns are numerically calculated from Eq. (16) at temperatures $T = 0.2$ K (blue), 0.3 K (yellow), and 0.5 K (green). The dotted curves are the analytical envelopes $2\bar{\Gamma}_q/\Gamma_1$ [cf., Eq. (49)]. (b) Oscillation produced by an out-of-plane magnetic field for a drum-like Fermi surface with $\mu = 0.12$ eV. The attenuation spike patterns are numerically calculated from Eq. (16) at temperatures $T = 0.5$ K (blue), 1.0 K (yellow), and 2.0 K (green). The dotted curves are the analytical envelopes $\bar{\Gamma}_q/\Gamma_1$ [cf., Eq. (49)]. (c) The numerical spike pattern (blue) and the analytical envelope (red) are exactly the same as the $T = 1.0$ K data in panel (b), expect for being plotted in a much wider range of ℓ_B^2. (d) Oscillation produced by an in-plane magnetic field for a torus Fermi surface with $\mu = 0.04$ eV. The attenuation spike patterns are numerically calculated from Eq. (31) at temperatures $T = 1.0$ K (blue), 2.0 K (yellow), and 3.0 K (green). The dotted curves are the analytical envelopes $\bar{\Gamma}'_q/\Gamma_2$ [cf., Eq. (52)].

the oscillating spike pattern can be similarly evaluated as

$$\tilde{\Gamma}'_q = \Gamma_2 \frac{\lambda\sqrt{M_0 M_1}}{2\mu\ell_B^2 k_B T}, \tag{52}$$

which is substantiated by its good match to the finite-temperature theory [Eq. (31)], as illustrated in Fig. 5(d). Again, we emphasize that Eq. (51) is only valid for the torus Fermi surface, while the form of phonon attenuation for the drum-like Fermi surface is not so analytically accessible due to the lack of analytic Landau level dispersions for $|\mu| > M_0$ in the presence of an in-plane magnetic field.

V. CONCLUSIONS AND DISCUSSIONS

We present a comprehensive analysis of the magnetoacoustic oscillation of phonon dispersion modification and the giant quantum oscillation of phonon attenuation in nodal-line semimetals at low temperature. Such phonon quantum oscillations are reminiscent of the Shubnikov-de Haas and de Haas-van Alphen oscillations of electrons in the nodal-line semimetals and serve as alternative experimental probes for the detection of Fermi-surface geometry. When the magnetic field is normal to the nodal-line plane, the phonon oscillations exhibit beating patterns for a torus Fermi surface. When the magnitude of the Fermi energy μ surpasses the model parameter M_0, the Fermi-surface topology changes. The resulting drum-like Fermi surface only possesses maximal cross section, leading to single-frequency phonon quantum oscillations. When the magnetic field is pointed parallel to the nodal-line plane, we analytically derive the Landau levels and show that the oscillations of topologically trivial phonons can acquire topologically nontrivial phase shift from electrons. Consequently, the phonon quantum oscillations not only offer discernible fingerprints for probing the Fermi-surface geometry and relativistic nature of nodal-line semimetals but also promote the comprehension of phonon physics in topological materials.

Our proposed phonon quantum oscillations can be detected with readily accessible experimental techniques. For example, the sound velocity modification and attenuation can be measured by pulse-echo phase sensitive detection technology [20,44,69–72].

More intriguingly, the phonon quantum oscillations have their own superiority over the electron quantum oscillations (e.g., the Shubnikov-de Haas and de Haas-van Alphen effects). In realistic materials, the inevitable smearing like finite-temperature effect, scattering, and non-negligible interactions can cause (i) a thermal damping factor $R_T = \lambda(T)/\sinh[\lambda(T)]$ with $\lambda(T) = j2\pi^2 m^* k_B T/(e\hbar B)$; and (ii) a Dingle damping factor $R_D = e^{-j\pi m^*/(eB\tau_q)}$, where m^* is the effective mass, τ_q is the lifetime, and j is the harmonic order. These two effects can smear out the higher-order harmonics. However, the giant quantum oscillation of phonon attenuation could provide the most abundant information of the higher-order harmonics [20]. Moreover, the lifetime of electronic bands would broaden the spikes of the phonon attenuation oscillation. The resulting spike width suggests a detectable temperature by comparing with the spike interval [43]. Lastly, the distinctive spike pattern at low temperature allows a more accurate identification of the field locations of the peaks of the oscillatory properties for the index plot. These features provide clear advantages of the phonon quantum oscillations over the electron quantum oscillations.

ACKNOWLEDGMENTS

The authors are indebted to S.-B. Zhang, S. Galesk, and C.-M. Wang for the insightful discussions. This work is supported by the National Key R&D Program of China (Grant No. 2022YFA1403700), the National Natural Science Foundation of China (Grants No. 11925402, No. 12304196, and No. 12350402), Guangdong Province (Grants No. 2020KCXTD001 and No. 2016ZT06D348), Guangdong Basic and Applied Basic Research Foundation (Grant No. 2022A1515111034), the Science, Technology and Innovation Commission of Shenzhen Municipality (Grants No. ZDSYS20170303165926217, No. JAY20170412152620376, and No. KYTDPT20181011104202253). The numerical calculations are supported by Center for Computational Science and Engineering of SUSTech.

APPENDIX A: FINITE-TEMPERATURE EFFECT

In Secs. IV A and IV B of the main text, finite temperature is incorporated into the phonon attenuation through convolution. Specifically, the convolution is done through

$$\tilde{\Gamma} = -\int_{-\infty}^{\infty} d\mathcal{E} \frac{\partial f(\mathcal{E})}{\partial \mathcal{E}} \Gamma(\mathcal{E}), \tag{A1}$$

where $\tilde{\Gamma}$ (Γ) is the attenuation at finite (zero) temperature and the derivative of the Fermi-Dirac distribution is $\partial f(\mathcal{E})/\partial\mathcal{E} = -1/[4k_BT]\cosh^{-2}[(\mathcal{E}-\mu)/(2k_BT)]$. Approaching the zero temperature, the derivative of Fermi-Dirac distribution is strongly peaked at $\mathcal{E} = \mu$, and the width of this peak depends on the temperature. Considering $\Gamma(\mathcal{E})$ adopts an oscillatory form as $\Gamma(\mathcal{E}) = H(\mathcal{E})\cos[\phi(\mathcal{E})]$, where $H(\mathcal{E})$ varies slowly with $\mathcal{E}$ and $\phi(\mathcal{E})$ changes rapidly with $\mathcal{E}$ [because of the large value of ℓ_B^2, see Eqs. (48), (50)], and (51)]. The convolution integral can be rewritten as

$$\tilde{\Gamma} = \frac{1}{4k_BT}\int_{-\infty}^{\infty} d\mathcal{E} \frac{H(\mathcal{E})\cos[\phi(\mathcal{E})]}{\cosh^2[(\mathcal{E}-\mu)/(2k_BT)]}, \tag{A2}$$

where the contribution of the denominator is only important near $\mathcal{E} = \mu$. We can thus move $H(\mathcal{E})$ out of the integral as $H(\mu)$, because it is a slowly varying function. Meanwhile, $\phi(\mathcal{E})$ oscillates rapidly and cannot be moved out as $\phi(\mu)$. We treat it by expanding to the first order of $\mathcal{E}-\mu$. With these assumptions, we find

$$\tilde{\Gamma} = H(\mu)\cos[\phi(\mu)]\frac{\kappa}{\sinh(\kappa)}, \tag{A3}$$

where $\kappa = \pi k_B T(\partial\phi/\partial\mathcal{E})_{\mathcal{E}=\mu}$. Making use of Eq. (A3) to the zero-temperature attenuation [Eq. (46)] leads to the finite-temperature attenuation [Eq. (47)].

APPENDIX B: CHEMICAL POTENTIAL WITH MAGNETIC FIELD DEPENDENCE

In the main text, we analyze the phonon quantum oscillations by fixing the chemical potential μ. In this Appendix, we perform numeric study to show that the phonon quantum oscillations persist even when μ acquires magnetic field dependence. We here focus on the out-of-plane magnetic field, while the in-plane magnetic field can be treated in a similar way.

In the presence of an out-of-plane magnetic field, we assume a fixed amount of charge carriers hosted by the Landau levels [Eq. (8)]. When the magnetic field is scanned, the carriers hosted by each Landau level varies, and the chemical potential changes accordingly [Figs. 6(a) and 6(c)]. The influence of magnetic-field-dependent chemical potential on the phonon quantum oscillations can be studied by performing substitution $\mu \to \mu(B)$ to our analytic theory [Eqs. (40), (41), (44), (48), (50), and (51)]. For example, in Figs. 6(b) and 6(d), we show beating and monochromatic magnetoacoustic oscillations for torus-shaped and drum-like Fermi surfaces, respectively.

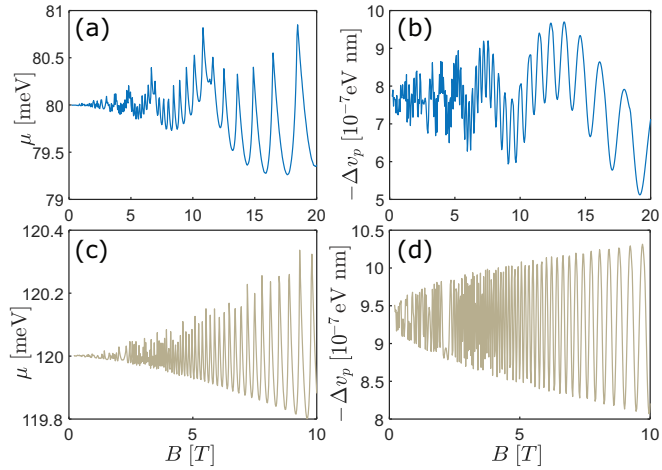

FIG. 6. The oscillations with a fixed amount of carriers under an out-of-plane magnetic field. Panels (a) and (b) exhibit beating behaviors associated with the torus-shaped Fermi surface, while panels (c) and (d) depict monochromatic oscillations associated with the drum-like Fermi surface.

[1] A. A. Burkov, M. D. Hook, and L. Balents, Topological nodal semimetals, Phys. Rev. B **84**, 235126 (2011).

[2] C.-K. Chiu and A. P. Schnyder, Classification of reflection-symmetry-protected topological semimetals and nodal superconductors, Phys. Rev. B **90**, 205136 (2014).

[3] B.-J. Yang, T. A. Bojesen, T. Morimoto, and A. Furusaki, Topological semimetals protected by off-centered symmetries in nonsymmorphic crystals, Phys. Rev. B **95**, 075135 (2017).

[4] C. Fang, H. Weng, X. Dai, and Z. Fang, Topological nodal line semimetals, Chin. Phys. B **25**, 117106 (2016).

[5] Y. Chen, Y. Xie, S. A. Yang, H. Pan, F. Zhang, M. L. Cohen, and S. Zhang, Nanostructured carbon allotropes with Weyl-like loops and points, Nano Lett. **15**, 6974 (2015).

[6] T. Bzdušek, Q. Wu, A. Rüegg, M. Sigrist, and A. A. Soluyanov, Nodal-chain metals, Nature (London) **538**, 75 (2016).

[7] C. Fang, Y. Chen, H.-Y. Kee, and L. Fu, Topological nodal line semimetals with and without spin-orbital coupling, Phys. Rev. B **92**, 081201(R) (2015).

[8] R. Yu, H. Weng, Z. Fang, X. Dai, and X. Hu, Topological node-line semimetal and Dirac semimetal state in antiperovskite Cu_3PdN, Phys. Rev. Lett. **115**, 036807 (2015).

[9] W. Chen, H.-Z. Lu, and O. Zilberberg, Weak localization and antilocalization in nodal-line semimetals: Dimensionality and topological effects, Phys. Rev. Lett. **122**, 196603 (2019).

[10] L. Muechler, A. Topp, R. Queiroz, M. Krivenkov, A. Varykhalov, J. Cano, C. R. Ast, and L. M. Schoop, Modular arithmetic with nodal lines: Drumhead surface states in ZrSiTe, Phys. Rev. X **10**, 011026 (2020).

[11] G.-Q. Zhao, S. Li, W. B. Rui, C. M. Wang, H.-Z. Lu, and X. C. Xie, 3D quantum Hall effect in a topological nodal-ring semimetal, Quantum Front. **2**, 22 (2023).

[12] G. Bian, T.-R. Chang, H. Zheng, S. Velury, S.-Y. Xu, T. Neupert, C.-K. Chiu, S.-M. Huang, D. S. Sanchez, I. Belopolski *et al.*, Drumhead surface states and topological nodal-line fermions in $TlTaSe_2$, Phys. Rev. B **93**, 121113(R) (2016).

[13] W. B. Rui, Y. X. Zhao, and A. P. Schnyder, Topological transport in Dirac nodal-line semimetals, Phys. Rev. B **97**, 161113(R) (2018).

[14] G. Bian, T.-R. Chang, R. Sankar, S.-Y. Xu, H. Zheng, T. Neupert, C.-K. Chiu, S.-M. Huang, G. Chang, I. Belopolski *et al.*, Topological nodal-line fermions in spin-orbit metal $PbTaSe_2$, Nat. Commun. **7**, 10556 (2016).

[15] L. M. Schoop, M. N. Ali, C. Straßer, A. Topp, A. Varykhalov, D. Marchenko, V. Duppel, S. S. Parkin, B. V. Lotsch, and C. R. Ast, Dirac cone protected by non-symmorphic symmetry and three-dimensional Dirac line node in ZrSiS, Nat. Commun. **7**, 11696 (2016).

[16] M. Neupane, I. Belopolski, M. M. Hosen, D. S. Sanchez, R. Sankar, M. Szlawska, S.-Y. Xu, K. Dimitri, N. Dhakal, P. Maldonado *et al.*, Observation of topological nodal fermion semimetal phase in ZrSiS, Phys. Rev. B **93**, 201104(R) (2016).

[17] C. Chen, X. Xu, J. Jiang, S.-C. Wu, Y. P. Qi, L. X. Yang, M. X. Wang, Y. Sun, N. B. M. Schröter, H. F. Yang, L. M. Schoop, Y. Y. Lv, J. Zhou, Y. B. Chen, S. H. Yao, M. H. Lu, Y. F. Chen, C. Felser, B. H. Yan, Z. K. Liu, and Y. L. Chen, Dirac line nodes and effect of spin-orbit coupling in the nonsymmorphic critical semimetals MSiS(M = Hf, Zr), Phys. Rev. B **95**, 125126 (2017).

[18] Y. Wu, L.-L. Wang, E. Mun, D. D. Johnson, D. Mou, L. Huang, Y. Lee, S. L. Bud'ko, P. C. Canfield, and A. Kaminski, Dirac node arcs in $PtSn_4$, Nat. Phys. **12**, 667 (2016).

[19] Y. Wang, H. F. Legg, T. Bömerich, J. Park, S. Biesenkamp, A. A. Taskin, M. Braden, A. Rosch, and Y. Ando, Gigantic magnetochiral anisotropy in the topological semimetal $ZrTe_5$, Phys. Rev. Lett. **128**, 176602 (2022).

[20] D. Shoenberg, *Magnetic Oscillations in Metals*, Cambridge Monographs on Physics (Cambridge University Press, Cambridge, 1984).

[21] R. Singha, A. K. Pariari, B. Satpati, and P. Mandal, Large nonsaturating magnetoresistance and signature of nondegenerate Dirac nodes in ZrSiS, Proc. Natl. Acad. Sci. USA **114**, 2468 (2017).

[22] M. N. Ali, L. M. Schoop, C. Garg, J. M. Lippmann, E. Lara, B. Lotsch, and S. S. P. Parkin, Butterfly magnetoresistance, quasi-2D Dirac Fermi surface and topological phase transition in ZrSiS, Sci. Adv. **2**, e1601742 (2016).

[23] X. Wang, X. Pan, M. Gao, J. Yu, J. Jiang, J. Zhang, H. Zuo, M. Zhang, Z. Wei, W. Niu *et al.*, Evidence of both surface and bulk Dirac bands and anisotropic nonsaturating magnetoresistance in ZrSiS, Adv. Electron. Mater **2**, 1600228 (2016).

[24] Y.-Y. Lv, B.-B. Zhang, X. Li, S.-H. Yao, Y. B. Chen, J. Zhou, S.-T. Zhang, M.-H. Lu, and Y.-F. Chen, Extremely large and significantly anisotropic magnetoresistance in ZrSiS single crystals, Appl. Phys. Lett **108**, 244101 (2016).

[25] H. Pan, B. Tong, J. Yu, J. Wang, D. Fu, S. Zhang, B. Wu, X. Wan, C. Zhang, X. Wang *et al.*, Three-dimensional anisotropic magnetoresistance in the Dirac node-line material ZrSiSe, Sci. Rep. **8**, 9340 (2018).

[26] J. Hu, Y. L. Zhu, D. Graf, Z. J. Tang, J. Y. Liu, and Z. Q. Mao, Quantum oscillation studies of the topological semimetal candidate ZrGeM(M = S, Se, Te), Phys. Rev. B **95**, 205134 (2017).

[27] N. Kumar, K. Manna, Y. Qi, S.-C. Wu, L. Wang, B. Yan, C. Felser, and C. Shekhar, Unusual magnetotransport from Si-square nets in topological semimetal HfSiS, Phys. Rev. B **95**, 121109(R) (2017).

[28] S. Pezzini, M. R. Van Delft, L. M. Schoop, B. V. Lotsch, A. Carrington, M. I. Katsnelson, N. E. Hussey, and S. Wiedmann, Unconventional mass enhancement around the Dirac nodal loop in ZrSiS, Nat. Phys. **14**, 178 (2018).

[29] H. Yang, R. Moessner, and L.-K. Lim, Quantum oscillations in nodal line systems, Phys. Rev. B **97**, 165118 (2018).

[30] M. R. van Delft, S. Pezzini, T. Khouri, C. S. A. Müller, M. Breitkreiz, L. M. Schoop, A. Carrington, N. E. Hussey, and S. Wiedmann, Electron-hole tunneling revealed by quantum oscillations in the nodal-line semimetal HfSiS, Phys. Rev. Lett. **121**, 256602 (2018).

[31] L. Guo, T.-W. Chen, C. Chen, L. Chen, Y. Zhang, G.-Y. Gao, J. Yang, X.-G. Li, W.-Y. Zhao, S. Dong *et al.*, Electronic transport evidence for topological nodal-line semimetals of ZrGeSe single crystals, ACS Appl. Electron. Mater. **1**, 869 (2019).

[32] M. Malasi, S. Rathod, A. Lakhani, and D. Kumar, Correlation induced instability in topological nodal-line semimetal ZrSiS, Appl. Phys. Lett. **123**, 093102 (2023).

[33] J. Hu, Z. Tang, J. Liu, Y. Zhu, J. Wei, and Z. Mao, Nearly massless Dirac fermions and strong Zeeman splitting in the nodal-line semimetal ZrSiS probed by de Haas-van Alphen quantum oscillations, Phys. Rev. B **96**, 045127 (2017).

[34] C. S. A. Müller, M. R. van Delft, T. Khouri, M. Breitkreiz, L. M. Schoop, A. Carrington, N. E. Hussey, and S. Wiedmann, Field-induced quasi-particle tunneling in the nodal-line semimetal HfSiS revealed by de Haas-van Alphen quantum oscillations, Phys. Rev. Res. **4**, 043008 (2022).

[35] F. Orbanić, M. Novak, Z. Glumac, A. McCollam, L. Tang, and I. Kokanović, Quantum oscillations of the magnetic torque in the nodal-line Dirac semimetal ZrSiS, Phys. Rev. B **103**, 045122 (2021).

[36] Y. H. Kwan, P. Reiss, Y. Han, M. Bristow, D. Prabhakaran, D. Graf, A. McCollam, S. A. Parameswaran, and A. I. Coldea, Quantum oscillations probe the Fermi surface topology of the nodal-line semimetal CaAgAs, Phys. Rev. Res. **2**, 012055(R) (2020).

[37] J. Hu, Z. Tang, J. Liu, X. Liu, Y. Zhu, D. Graf, K. Myhro, S. Tran, C. N. Lau, J. Wei *et al.*, Evidence of topological nodal-line fermions in ZrSiSe and ZrSiTe, Phys. Rev. Lett. **117**, 016602 (2016).

[38] I. M. Lifshitz and A. M. Kosevich, On the theory of magnetic susceptibility of metals at low temperatures, Zh. Eksp. Teor. Fiz. **29**, 730 (1955).

[39] H. Murakawa, M. S. Bahramy, M. Tokunaga, Y. Kohama, C. Bell, Y. Kaneko, N. Nagaosa, H. Y. Hwang, and Y. Tokura, Detection of Berry's phase in a bulk Rashba semiconductor, Science **342**, 1490 (2013).

[40] M. Matusiak, J. Cooper, and D. Kaczorowski, Thermoelectric quantum oscillations in ZrSiS, Nat. Commun. **8**, 15219 (2017).

[41] X. Xu, Z. Kang, T.-R. Chang, H. Lin, G. Bian, Z. Yuan, Z. Qu, J. Zhang, and S. Jia, Quantum oscillations in the noncentrosymmetric superconductor and topological nodal-line semimetal $PbTaSe_2$, Phys. Rev. B **99**, 104516 (2019).

[42] T. Osada, T. Ochi, and T. Taen, Thermoelectric Hall effect at high-magnetic-field quantum limit in graphite as a nodal-line semimetal, J. Phys. Soc. Jpn. **91**, 063701 (2022).

[43] S.-B. Zhang and J. Zhou, Quantum oscillations in acoustic phonons in Weyl semimetals, Phys. Rev. B **101**, 085202 (2020).

[44] C. Schindler, D. Gorbunov, S. Zherlitsyn, S. Galeski, M. Schmidt, J. Wosnitza, and J. Gooth, Strong anisotropy of the electron-phonon interaction in NbP probed by magnetoacoustic quantum oscillations, Phys. Rev. B **102**, 165156 (2020).

[45] S. Galeski, T. Ehmcke, R. Wawrzyńczak, P. M. Lozano, K. Cho, A. Sharma, S. Das, F. Küster, P. Sessi, M. Brando, and others, Origin of the quasi-quantized Hall effect in $ZrTe_5$, Nat. Commun. **12**, 3197 (2021).

[46] T. Ehmcke, S. Galeski, D. Gorbunov, S. Zherlitsyn, J. Wosnitza, J. Gooth, and T. Meng, Propagation of longitudinal acoustic phonons in $ZrTe_5$ exposed to a quantizing magnetic field, Phys. Rev. B **104**, 245117 (2021).

[47] S. Galeski, K. Araki, O. K. Forslund, R. Wawrzynczak, H. F. Legg, P. K. Sivakumar, U. Miniotaite, F. Elson, M. Månsson, C. Witteveen, and others, Anomalous Shubnikov-de Haas effect and observation of the Bloch-Gruneisen temperature in the Dirac semimetal $ZrTe_5$, arXiv:2309.10480.

[48] B. Bermond, R. Wawrzynczak, S. Zherlitsyn, T. Kotte, T. Helm, D. Gorbunov, G. D. Gu, Q. Li, F. Janasz, T. Meng *et al.*, Giant quantum oscillations in thermal transport in low-density metals via electron absorption of phonons, arXiv:2402.17022.

[49] Y. Liu, G. Dhakal, A. P. Sakhya, J. E. Beetar, F. Kabir, S. Regmi, D. Kaczorowski, M. Chini, B. M. Fregoso, and M. Neupane, Ultrafast relaxation of acoustic and optical phonons in a topological nodal-line semimetal ZrSiS, Commun. Phys. **5**, 203 (2022).

[50] A. N. Rudenko and S. Yuan, Electron-phonon interaction and zero-field charge carrier transport in the nodal-line semimetal ZrSiS, Phys. Rev. B **101**, 115127 (2020).

[51] Z. Zhou, X. Yang, H. Wang, G. Han, X. Lu, G. Wang, R. Wang, and X. Zhou, Giant phonon anomaly in topological nodal-line semimetals, Funda. Res. (2022), doi:10.1016/j.fmre.2022.12.012.

[52] W. Zhou, H. Gao, J. Zhang, R. Fang, H. Song, T. Hu, A. Stroppa, L. Li, X. Wang, S. Ruan *et al.*, Lattice dynamics of Dirac node-line semimetal ZrSiS, Phys. Rev. B **96**, 064103 (2017).

[53] B. Salmankurt and S. Duman, First-principles study of structural, mechanical, lattice dynamical and thermal properties of nodal-line semimetals ZrXY (X = Si, Ge; Y = S, Se), Philos. Mag. **97**, 175 (2017).

[54] R. Singha, S. Samanta, S. Chatterjee, A. Pariari, D. Majumdar, B. Satpati, L. Wang, A. Singha, and P. Mandal, Probing lattice dynamics and electron-phonon coupling in the topological nodal-line semimetal ZrSiS, Phys. Rev. B **97**, 094112 (2018).

[55] S. Xue, T. Zhang, C. Yi, S. Zhang, X. Jia, L. H. Santos, C. Fang, Y. Shi, X. Zhu, and J. Guo, Electron-phonon coupling and Kohn anomaly due to floating two-dimensional electronic bands on the surface of ZrSiS, Phys. Rev. B **100**, 195409 (2019).

[56] B. Fu, H.-W. Wang, and S.-Q. Shen, Dirac polarons and resistivity anomaly in $ZrTe_5$ and $HfTe_5$, Phys. Rev. Lett. **125**, 256601 (2020).

[57] T. Ikenobe, T. Yamada, D. Hirai, H. Yamane, and Z. Hiroi, Superconductivity induced by doping holes in the nodal-line semimetal NaAlGe, Phys. Rev. Mater. **7**, 104801 (2023).

[58] C. Li, C. M. Wang, B. Wan, X. Wan, H.-Z. Lu, and X. C. Xie, Rules for phase shifts of quantum oscillations in topological nodal-line semimetals, Phys. Rev. Lett. **120**, 146602 (2018).

[59] K. Mullen, B. Uchoa, and D. T. Glatzhofer, Line of Dirac nodes in hyperhoneycomb lattices, Phys. Rev. Lett. **115**, 026403 (2015).

[60] Y. Kim, B. J. Wieder, C. L. Kane, and A. M. Rappe, Dirac line nodes in inversion-symmetric crystals, Phys. Rev. Lett. **115**, 036806 (2015).

[61] J. M. Ziman, *Electrons and Phonons: The Theory of Transport Phenomena in Solids* (Oxford University Press, Oxford, 2001).

[62] G. D. Mahan, *Many-Particle Physics*, Physics of Solids and Liquids (Springer, New York, 2000).

[63] With a typical ℓ_B^2 magnitude of 10^2, the the Landau level energy gap $\hbar\omega$ is on the order of 10^{-4}eV. Consequently, this gap is larger by two orders of magnitude compared to the phonon energy $\Omega_q \approx 3.9 \times 10^{-6}$eV.

[64] T. Liu and H.-Z. Lu, Analytic solution to pseudo-Landau levels in strongly bent graphene nanoribbons, Phys. Rev. Res. **4**, 023137 (2022).

[65] Z. Shi, H.-Z. Lu, and T. Liu, Pseudo Landau levels, negative strain resistivity, and enhanced thermopower in twisted graphene nanoribbons, Phys. Rev. Res. **3**, 033139 (2021).

[66] T. Liu and Z. Shi, Strain-induced dispersive landau levels: Application in twisted honeycomb magnets, Phys. Rev. B **103**, 144420 (2021).

[67] A. Abrikosov, *Fundamentals of the Theory of Metals* (Dover Publications, New York, 2017).

[68] The phase $\pm\pi/4$ in Eq. (40) is originated from the quantum oscillation of 3D electrons. In 3D nonmagnetic metals, the phase shift of the electron quantum oscillations in general reads $\phi = \phi_M + \phi_B + \phi_{3D}$, where $\phi_M = -\pi$ is the Maslov phase [73], ϕ_B is the Berry phase [74–76], and $\phi_{3D} = \pm\pi/4$ relies on the geometry of Fermi surface and the carrier type. Specifically, $\phi_{3D} = \pi/4$ is adopted for the minimal cross-section of electrons, while $\phi_{3D} = -\pi/4$ is adopted for the maximal cross section of electrons [38,58,67,77,78]. And holes are assigned opposite values when the Landau index is taken as negative as some experimental convension assigns negative Landau level indices for holes elaborated in Refs. [27,40,41,58,78–87].

[69] Y. Shapira and B. Lax, Line shape and amplitude of giant quantum oscillations in ultrasonic absorption, Phys. Rev. **138**, A1191 (1965).

[70] B. Lüthi, *Physical Acoustics in the Solid State*, Vol. 148 (Springer, Berlin, 2007).

[71] B. Wolf, B. Lüthi, S. Schmidt, H. Schwenk, M. Sieling, S. Zherlitsyn, and I. Kouroudis, New experimental techniques for pulsed magnetic fields–ESR and ultrasonics, Phys. B **294-295**, 612 (2001).

[72] L. Testardi and J. Condon, 2 – Landau quantum oscillations of the velocity of sound and the strain dependence of the Fermi surface, Phys. Acoust. **8**, 59 (1971).

[73] J. N. Fuchs, F. Piéchon, M. O. Goerbig, and G. Montambaux, Topological Berry phase and semiclassical quantization of cyclotron orbits for two dimensional electrons in coupled band models, Eur. Phys. J. B **77**, 351 (2010).

[74] G. P. Mikitik and Y. V. Sharlai, Manifestation of Berry's phase in metal physics, Phys. Rev. Lett. **82**, 2147 (1999).

[75] D. Xiao, M.-C. Chang, and Q. Niu, Berry phase effects on electronic properties, Rev. Mod. Phys. **82**, 1959 (2010).

[76] H.-J. Lin, H.-P. Sun, T. Liu, and P.-L. Zhao, Tuning three-dimensional higher-order topological insulators by surface state hybridization, Phys. Rev. B **108**, 165427 (2023).

[77] M. V. Kartsovnik, High magnetic fields: A tool for studying electronic properties of layered organic metals, Chem. Rev. **104**, 5737 (2004).

[78] C. M. Wang, H.-Z. Lu, and S.-Q. Shen, Anomalous phase shift of quantum oscillations in 3D topological semimetals, Phys. Rev. Lett. **117**, 077201 (2016).

[79] R. Chapai, D. Browne, D. E. Graf, J. DiTusa, and R. Jin, Quantum oscillations with angular dependence in $PdTe_2$ single crystals, J. Phys.: Condens. Matter **33**, 035601 (2021).

[80] J. Liu, P. Liu, K. Gordon, E. Emmanouilidou, J. Xing, D. Graf, B. C. Chakoumakos, Y. Wu, H. Cao, D. Dessau *et al.*, Nontrivial topology in the layered Dirac nodal-line semimetal candidate $SrZnSb_2$ with distorted Sb square nets, Phys. Rev. B **100**, 195123 (2019).

[81] E. Emmanouilidou, S. Mardanya, J. Xing, P. V. S. Reddy, A. Agarwal, T.-R. Chang, and N. Ni, Fermiology and type-I superconductivity in the chiral superconductor $NbGe_2$ with Kramers-Weyl fermions, Phys. Rev. B **102**, 235144 (2020).

[82] M.-X. Yang, W. Luo, and W. Chen, Quantum transport in topological nodal-line semimetals, Adv. Phys.: X **7**, 2065216 (2022).

[83] L. Xing, R. Chapai, R. Nepal, and R. Jin, Topological behavior and Zeeman splitting in trigonal $PtBi_{2-x}$ single crystals, npj Quantum Mater. **5**, 10 (2020).

[84] O. Pavlosiuk and D. Kaczorowski, Galvanomagnetic properties of the putative type-II Dirac semimetal $PtTe_2$, Sci. Rep. **8**, 11297 (2018).

[85] R. Chapai, P. V. S. Reddy, L. Xing, D. E. Graf, A. B. Karki, T.-R. Chang, and R. Jin, Evidence for unconventional superconductivity and nontrivial topology in PdTe, Sci. Rep. **13**, 6824 (2023).

[86] Y. Zhang, Y.-W. Tan, H. L. Stormer, and P. Kim, Experimental observation of the quantum Hall effect and Berry's phase in graphene, Nature (London) **438**, 201 (2005).

[87] G. Eguchi, K. Kuroda, K. Shirai, A. Kimura, and M. Shiraishi, Surface Shubnikov–de Haas oscillations and nonzero Berry phases of the topological hole conduction in $Tl_{1-x}Bi_{1+x}Se_2$, Phys. Rev. B **90**, 201307(R) (2014).